nature portfolio

https://doi.org/10.1038/s41586-026-10804-0

Supplementary information

Programming fracture resistance in metamaterials via elastic instabilities

In the format provided by the authors and unedited

Supplementary Information for

Programming Fracture Resistance in Metamaterials via Elastic Instabilities

Yujia Wang[1,2], Yangchengyi Liu[2], Kunlin Wu[2], Xuan Zhang[1], Hanzheng Xing[1], Songyan Zhang[1], Changhong Linghu[2], Yifan Wang[2], Xiaoyan Li[1,*], and Huajian Gao[1,*]

[1]Mechano-X Institute, Applied Mechanics Laboratory, Department of Engineering Mechanics, Tsinghua University, Beijing 100084, China

[2]School of Mechanical and Aerospace Engineering, College of Engineering, Nanyang Technological University, 70 Nanyang Drive, Singapore 639798, Singapore

***Corresponding Authors:** xiaoyanlithu@tsinghua.edu.cn (X.L.), gao.huajian@tsinghua.edu.cn (H.G.).

This PDF file includes:

Supplementary Note 1

To gain a deeper understanding of the intrinsic-to-extrinsic transition in fracture behaviors of these snap-through metamaterials and to explore regimes beyond experimental limitations, we developed a theoretical model to predict the inelastic zone size and fracture energy.

We first derive the stress-strain relationships of metamaterials composed of n_h layers of unit cells in the loading direction, based on the mechanical behaviors of the unit cell, following procedures in previous studies[1,2]. To ensure high accuracy, the mechanical behaviors of the unit cells were obtained through finite element (FE) simulations with periodical boundary conditions. For example, the stress-strain relationship and the local maximum principal strain during loading for the unit cell with t_s/l=0.10 are presented in Fig. S4a,b, and are described as

$$\sigma = \sigma^{uc}\left(\varepsilon\right),\ \varepsilon_{\max} = \varepsilon_{\max}^{uc}\left(\varepsilon\right) \tag{S1}$$

where σ and ε are the effective stress and strain along the loading direction of the unit cell, while $\varepsilon_{\max}$ denotes the local maximum principal strain in the unit cell, occurring at the intersection of the thinner curved beam and the vertical support part of the unit cell. The stress-strain curve features two points with zero tangential stiffness, $\left(\varepsilon_I, \sigma_I\right)$ and $\left(\varepsilon_{II}, \sigma_{II}\right)$, leading to a breakdown of the one-to-one mapping between stress and strain in the regime $\sigma_{II} < \sigma < \sigma_I$. There are two regions with positive tangential stiffness: Region I for $\varepsilon < \varepsilon_I$, and Region II for $\varepsilon > \varepsilon_{II}$, separated by a spinodal region $\varepsilon_I < \varepsilon < \varepsilon_{II}$ (Fig. S4a). We consider a lattice composed of periodically arranged unit cells, with n_h representing the number of unit cells along the loading direction. The effective stress and strain of the lattice are given by

$$\bar{\sigma} = \sigma^{(i)},\ i = 1, 2, \cdots, n_h \tag{S2}$$

$$\bar{\varepsilon} = \frac{1}{n_h}\sum_{i=1}^{n_h} \varepsilon^{(i)},\ i = 1, 2, \cdots, n_h \tag{S3}$$

where $\sigma^{(i)}$ and $\varepsilon^{(i)}$ are the stress and strain of the ith unit cell, respectively, and satisfy the

numerical stress-strain relationship of the unit cell shown in Fig. S4a, $\sigma^{(i)} = \sigma^{uc}\left(\varepsilon^{(i)}\right)$. For any given $\bar{\sigma}$, we can determine the effective strain of each unit cell ε_i and then obtain the effective strain of the lattice $\bar{\varepsilon}$ using Eq. S3.

This process is straightforward when $\bar{\sigma} > \sigma_I$ or $\bar{\sigma} < \sigma_{II}$, as only a unique strain corresponds to the given stress $\sigma_i = \bar{\sigma}$ of the unit cell. However, for $\sigma_{II} < \bar{\sigma} < \sigma_I$, there are multiple strains corresponding to the given stress. In this case, all possible stable equilibrium configurations must be identified. We use $\left(n_I, n_{II}, n_S\right)$ to describe the configuration of the lattice, where n_I, n_{II}, and n_S represent the number of unit cells in Region I, Region II, and the spinodal region, respectively ($n_I+n_{II}+n_S=n_h$). In this study, we consider only mechanically stable equilibrium configurations with $n_S=0$. Detailed discussions on stable and unstable equilibrium configurations, along with their conditions, can be found in previous studies[1–3].

For a given $\bar{\sigma}$ in the range $\sigma_{II} < \bar{\sigma} < \sigma_I$, two corresponding strains of the unit cell can be determined: ε_1 in Region I and ε_2 in Region II (Fig. S4a). The corresponding strain energy densities, w_1 and w_2, are obtained by integrating the stress-strain curve of the unit cell. The effective strain and the average strain energy density of the lattice are expressed as

$$\bar{\varepsilon} = \frac{\left(n_h - n_{II}\right)\varepsilon_1 + n_{II}\varepsilon_2}{n_h} \tag{S4}$$

$$\bar{w} = \frac{\left(n_h - n_{II}\right)w_1 + n_{II}w_2}{n_h} \tag{S5}$$

We obtain n_h+1 stable branches for $n_{II} = 0, 1, \cdots, n_h$. The stress-strain relationship of the lattice is shown in Fig. 1h of the main text.

Next, we consider a lattice with a precrack (Fig. S4c). The energy release rate G is determined by the difference in energy stored far ahead of and far behind the crack tip, i.e.

$$G = n_h \cdot h \cdot \left(w_\infty - w_{-\infty} \right) \tag{S6}$$

where h is the height of the unit cell, and $w_{-\infty} = 0$ for our sample. By rewriting Eq. S6, we obtain

$$G = n_h \cdot h \cdot \bar{w} = h \cdot \left[\left(n_h - n_{iz} \right) w_1 + n_{iz} w_2 \right] \tag{S7}$$

where $\bar{w}$ is the average strain energy density far ahead of the crack tip, n_{iz} is the inelastic zone size defined as the number of unit cell layers where instabilities have been triggered, and w_1 and w_2 are the strain energy densities of unit cells outside and inside the inelastic zone, respectively. For a given stress $\bar{\sigma}$ far ahead of the crack tip, we can obtain ε_1, ε_2, w_1, and w_2 from the stress-strain relationship of the unit cell and then calculate the corresponding lattice strain and energy release rate using Eqs. S4 and S7. The relationship between the derived energy release rate and strain is presented in Fig. S4d.

Then, we determine the critical energy release rate based on the maximum principal strain criterion. The applied stress intensity factor is expressed as $K_{applied} = \sqrt{EG}$, where E is the modulus of the lattice structure, obtained from Fig. 1h. The triggered instabilities can be considered as a phase transformation that relaxes stress around the crack tip and reduces the crack-tip stress intensity factor[4]. Therefore,

$$K_{tip} = K_{applied} - \Delta K \tag{S8}$$

where ΔK is the contribution from the transformations and is given by[4]

$$\Delta K = A' E \varepsilon_T \sqrt{n_{iz} h / 2} \tag{S9}$$

where $A' = 0.22/\left(1-\nu\right)$ is a constant, and ε_T is the transformation strain, defined as the inelastic strain corresponding to the second stage of the stress-strain curve. According to linear elastic fracture mechanics (LEFM)[5], under the assumption of a continuous medium, a singular stress field would develop ahead of the crack tip, in the form of

$$\sigma = \frac{K_{tip}}{\sqrt{2\pi r}} \tag{S10}$$

where r is the distance from the crack tip. We assume that the unit cell at the crack tip is subjected to a force expressed as[6]

$$F = \int_0^l \frac{K_{tip}}{\sqrt{2\pi r}} b \mathrm{d}r \tag{S11}$$

where b is the out-of-plane thickness. The effective stress of the unit cell at the crack tip is given by

$$\bar{\sigma}_{tip} = \frac{F}{l \cdot b} \tag{S12}$$

Using the stress-strain relationship of the unit cell (Fig. S4a), the effective strain of the unit cell at the crack tip, $\bar{\varepsilon}_{tip}$, can be determined. Note that for $n_{iz} \geq 1$, the corresponding strain in Region II is used, as instabilities always initiate at the crack tip. Based on $\bar{\varepsilon}_{tip}$, the local maximum principal strain is extracted from the unit cell behavior (Fig. S4b). The derived local maximum principal strain of the lattice during loading is shown in Fig. S4e.

Therefore, for a given fracture strain of the constituent material, ε_{fs}, we can determine the critical strain ε_{cr} of the lattice for crack initiation, the corresponding inelastic zone size n_{iz} (Fig. S4e), and subsequently the critical energy release rate (Fig. S4d).

Following the above procedure, we derived Fig. 4i-k in the main text. The resulting phase diagram (Fig. 4i) clearly presents the boundary of the extrinsic regime. Since this procedure predicts n_{iz} across the entire parameter space, it implicitly includes the critical condition for extrinsic fracture behavior ($n_{iz}=n_h$). The critical condition can also be explicitly examined as a special case of the general procedure, as described below.

The critical condition can be stated as follows: once the inelastic zone reaches the boundary, the unit cell at the crack tip attains its fracture strength. At this point, $K_{applied}$ and K_{tip} reach their respective critical values. By rewriting Eq. S8, we obtained

$$K_{tip}^{(0)} = \sqrt{EG_{cr}} - A' E \varepsilon_T \sqrt{n_h h/2} \tag{S13}$$

The unit cells far ahead of the crack tip are in the state of $\left(\varepsilon_I+\varepsilon_T,\sigma_I\right)$, as shown in Fig. S4a, and their strain energy density is denoted by w_T. The corresponding critical energy release rate is then given by,

$$G_{cr}=n_h\cdot h\cdot w_T \tag{S14}$$

According to Eqs. S10-S12,

$$K_{tip}^{(0)}=\sigma_f\sqrt{\frac{\pi l}{2}} \tag{S15}$$

where σ_f is the fracture strength of the unit cell, determined by its mechanical behavior and the material fracture strain ε_{fs} (Fig. S4a-b). Substituting Eqs. S14 and S15 into Eq. S13, the critical condition can be expressed as,

$$\frac{\sigma_f}{E\varepsilon_T}\sqrt{\frac{\pi l}{n_h h}}=\sqrt{\frac{2w_T}{E\varepsilon_T{}^2}}-A' \tag{S16}$$

In Eq. S16, E, w_T, and ε_T depend on the unit cell geometry (t_s/l) for a given material constitutive law, while σ_f depends on both t_s/l and ε_{fs}. This equation defines the boundary of the extrinsic regime in the phase diagram (Fig. 4i).

The predicted fracture energy in the extrinsic regime is slightly lower than the experimental results (Fig.4j,k), which we attribute to an underestimation of the contribution from transformation toughening. Since the metamaterial in the extrinsic regime exhibits a large transformation zone extending across the entire sample, the estimation of the crack-tip shielding effect using the classical theory (Eq. S9) with a constant $A'=0.22/\left(1-\nu\right)$ provides a relatively conservative prediction and could be regarded as a lower bound.

Additionally, by combining Eqs. S8 and S9, we obtained the relationship between the energy release rate and the inelastic zone size:

$$\sqrt{G}=K_{tip}\Big/\sqrt{E}+A'\varepsilon_T\sqrt{En_{iz}h/2} \tag{S17}$$

Therefore, for metamaterials exhibiting extrinsic fracture toughness, $n_{iz}=n_h=n_w/2$. The fracture energy scales with sample size as

$$\sqrt{\Gamma} = K_{tip}^{(0)} \Big/ \sqrt{E} + \sqrt{n_w} \cdot A' \varepsilon_T \sqrt{Eh} \Big/ 2 = C_1 \sqrt{n_w} + C_2 \quad \text{(S18)}$$

We calculated the fracture energies of metamaterials with sample sizes up to n_w=2,000, with the results presented in Fig. S5. For a given material's fracture strain large enough to ensure all samples remain in the extrinsic regime, the fracture energy increases monotonically with sample size, as described by Eq. S18.

We applied this scaling law to fit the experimental data for 2D curved-beam metamaterials across scales (Fig. 4l; Extended Data Figs. 6c and 7d) as well as 3D straw-like shell-based metamaterials (Extended Data Fig. 8e). The fitted values of C_1 and C_2 are summarized in Supplementary Table 1. The 3D shell-based architectures exhibit a smaller C_2 value than 2D curved-beam metamaterials fabricated from TPU, because their fracture is governed by interlayer delamination between printed filaments, whereas the 2D curved-beam samples fail through tensile rupture along the filaments. These results indicate that Eq. S18 provides a generalized scaling law for the fracture energy of snap-through metamaterials in the extrinsic regime.

Supplementary Note 2

To isolate and clearly demonstrate the instability-mediated fracture mechanism, we employed 2D curved-beam metamaterials in the main text. We emphasize that the underlying mechanism is not limited to specific architectures or loading conditions. From a mechanics perspective, this mechanism is governed by the activation of elastic instability ahead of the crack tip and the resulting inelastic zone expansion and associated energy dissipation. These processes can be implemented across different scales, architectures, loading conditions, and dimensionalities.

We have demonstrated the applicability of the mechanism to larger and smaller scales (Extended Data Figs. 6-7), and to different architectures such as straw-like shell-based geometries (Extended Data Fig. 8). Here, we further demonstrate its extensions to mixed-mode loading, more general 2D architectures exhibiting snap-through instabilities along diagonal directions, as well as 3D tri-directional snap-through architectures.

We first introduced inclined precracks into the 2D curved-beam metamaterials fabricated from TPU via FDM, and subjected the samples to uniaxial tension. The inclined cracks experience combined Mode-I and Mode-II loading, representing a classical mixed-mode configuration. As shown in Fig. S7a, elastic instability is still first activated near the crack tip and subsequently spreads across the sample prior to crack propagation. After fracture initiation, the crack propagates normal to the applied load, consistent with classical fracture mechanics, wherein mixed-mode cracks tend to evolve toward Mode I during loading. We also observed that this behavior is insensitive to the inclined angle of the precrack (Fig. S7b-e).

To effectively activate snap-through instabilities, the instability direction was arranged along the loading direction. To validate the robustness of the mechanism, we designed a 2D unit cell composed of curved beams that exhibits snap-through instabilities along two diagonal directions that are not aligned with the vertical applied loading (Extended Data Fig. 9a). In this more general architecture, instability is still activated from the crack tip, leading to the growth of an inelastic zone that extends to the sample boundaries prior to crack propagation (Extended Data Fig. 9b,d). To quantitatively characterize the fracture energy of these metamaterials, we employed the same standard protocol as in the main text (Fig. S8a), with results showing an increase in fracture energy with increasing sample size (Fig. S8c-d).

We performed additional FE simulations on these bidirectional metamaterials to investigate their fracture behaviors under biaxial tension (Fig. S9). As shown in Fig. S9d, under biaxial loading, snap-through instabilities are still triggered from the crack tip along both principal directions and subsequently spread across the sample, confirming that the mechanism operates under bidirectional loading. The critical displacement, x_{cr}, is defined as the point at which the local maximum principal strain reaches the fracture strain of the base material. To determine the fracture energy, we introduced a reference sample (Fig. S9e) of the same width but with a larger crack length which was loaded to the same displacement x_{cr}. The difference in strain energy

between the two samples at this displacement was used to calculate the fracture energy (Fig. S9f),

$$\Gamma = -\frac{U\left(a+\Delta a\right)-U\left(a\right)}{B\cdot 2\Delta a}$$

where B is the out-of-plane thickness, and $B\cdot\left(2\Delta a\right)=B\cdot\left(2l_{2d}\right)$ represents the crack area increment. Following this procedure, we calculated fracture energy for samples with different sizes ($2W$=6l_{2d}, 12l_{2d}, and 18l_{2d}), while maintaining a/W=1/3. As shown in Fig. S9g, the fracture energy increases with sample size, consistent with the observations under uniaxial loading. This demonstrates that similar extrinsic fracture behaviors can also be achieved in bidirectional snap-through metamaterials under biaxial tension.

We further performed FE simulations on 3D tri-directional snap-through metamaterials with embedded square cracks. We investigated two types of unit cells that exhibit snap-through instabilities either aligned or not aligned with the loading direction (Figs. S10-11). Under uniaxial loading, elastic instability is similarly triggered in the vicinity of the crack tip, followed by expansion of an inelastic zone prior to crack growth. We also examined more general cases with inclined embedded cracks under tri-directional tension loading, with results confirming the same qualitative behavior (Fig. S12).

In summary, the foundational principle that elastic instabilities can be deliberately harnessed to program fracture resistance broadly applies across different scales, architectures, loading conditions, and dimensionalities. By explicitly bridging two traditionally distinct failure phenomena—elastic instability and fracture—this study introduces a new pathway for regulating fracture processes. Different geometries, boundary conditions, and crack configurations can be employed to tailor the size, shape, and evolution of inelastic zones, enabling programmable fracture behaviors across a wide range of systems.

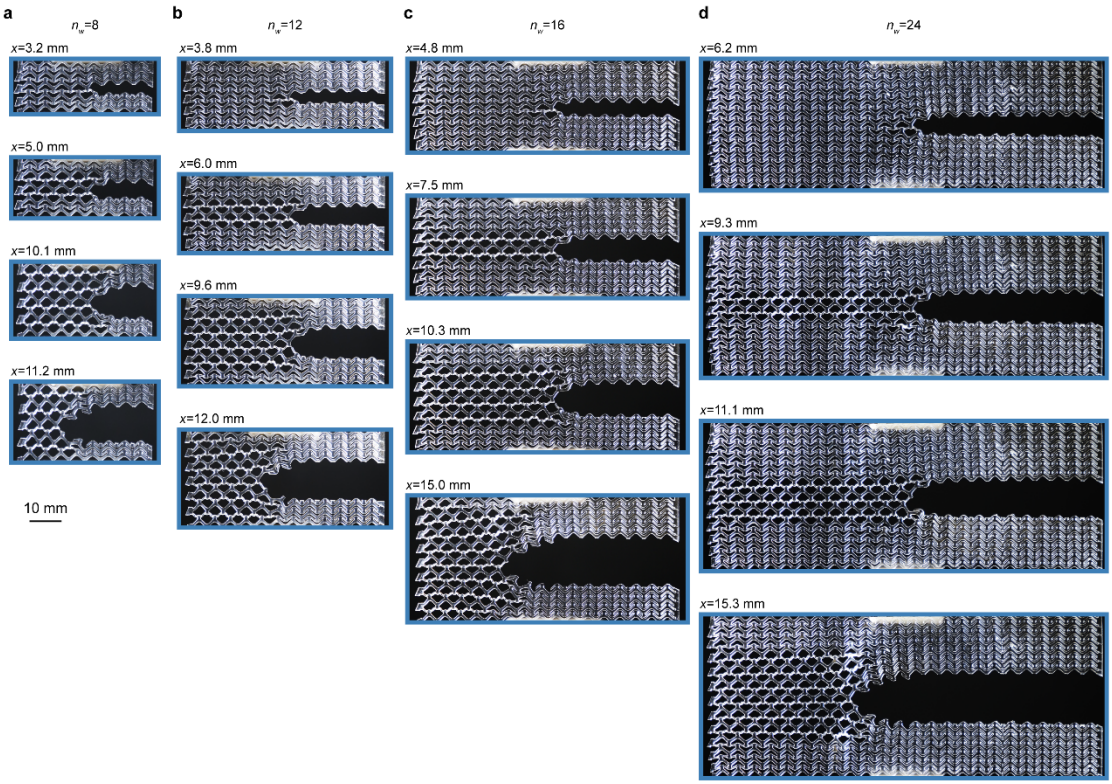

Supplementary Fig. 1 | Snapshots during loading of metamaterials with t_s/l=0.12, fabricated at T_2=150°C. a-d, Snapshots for samples with n_w=8, n_w=12, n_w=16, and n_w=24, respectively. In each panel, the first two images illustrate the deformation configurations prior to fracture initiation, showing instabilities triggered in one unit cell and two layers of unit cells, respectively. The third image corresponds to the moment of fracture initiation. The final row shows an image during crack propagation at a later stage.

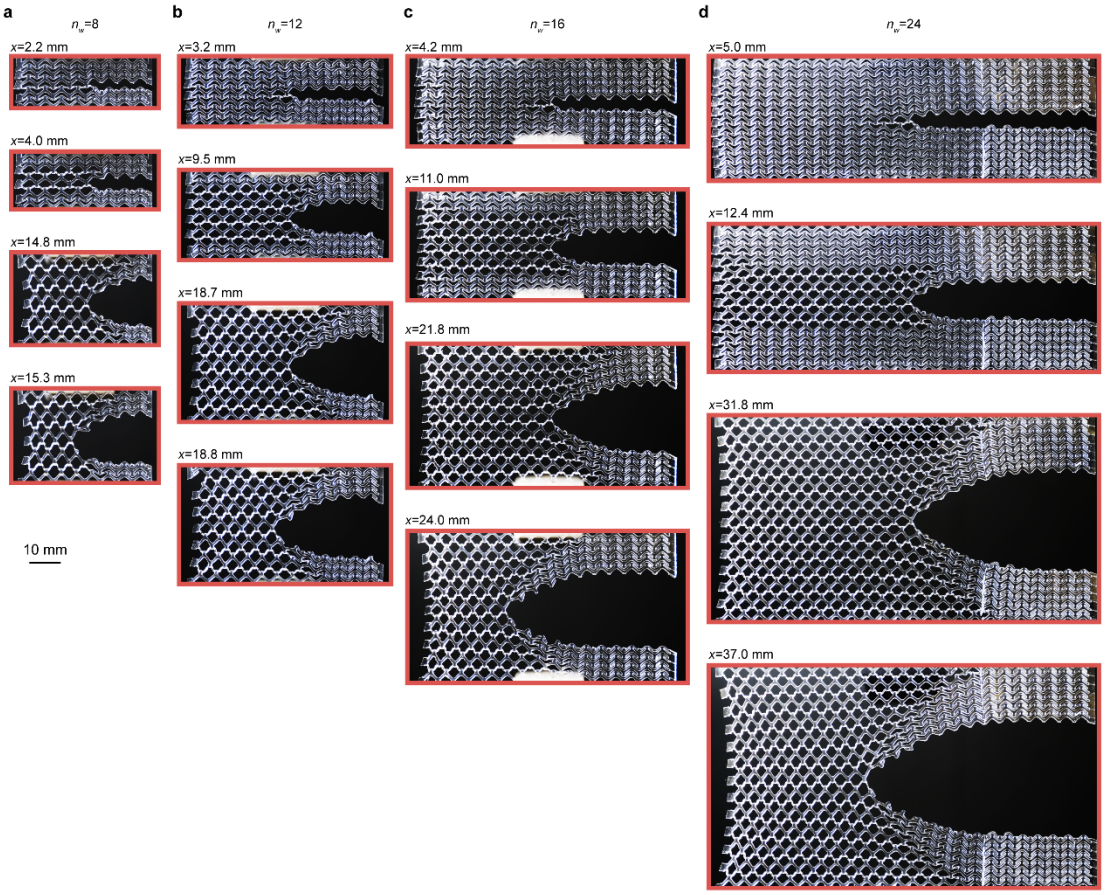

Supplementary Fig. 2 | Snapshots during loading of metamaterials with t_s/l=0.10, fabricated at T_2=70°C. a-d, Snapshots for samples with n_w=8, n_w=12, n_w=16, and n_w=24, respectively. In each panel, the first two images illustrate the deformation configurations prior to fracture initiation, showing instabilities triggered in one unit cell and two layers of unit cells (a) or four layers of unit cells (b-d). The third image corresponds to the moment of fracture initiation, where instabilities have already spread to the sample boundary. The final row shows an image during crack propagation at a later stage.

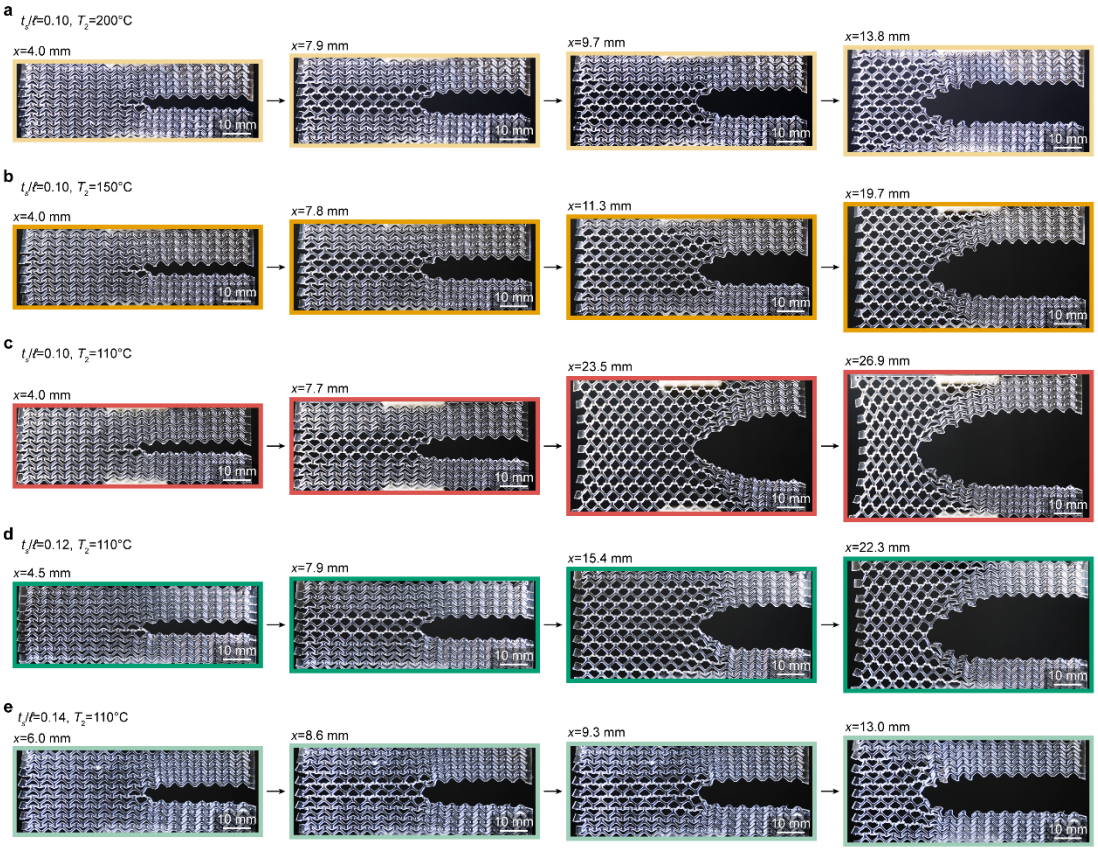

Supplementary Fig. 3 | Snapshots during loading of metamaterials showing intrinsic-to-extrinsic transition. a, Snapshots of a metamaterial with t_s/l=0.10, fabricated at T_2=200°C. **b**, Snapshots of a metamaterial with t_s/l=0.10, fabricated at T_2=150°C. **c**, Snapshots of a metamaterial with t_s/l=0.10, fabricated at T_2=110°C. **d**, Snapshots of a metamaterial with t_s/l=0.12, fabricated at T_2=110°C. **e**, Snapshots of a metamaterial with t_s/l=0.14, fabricated at T_2=110°C.

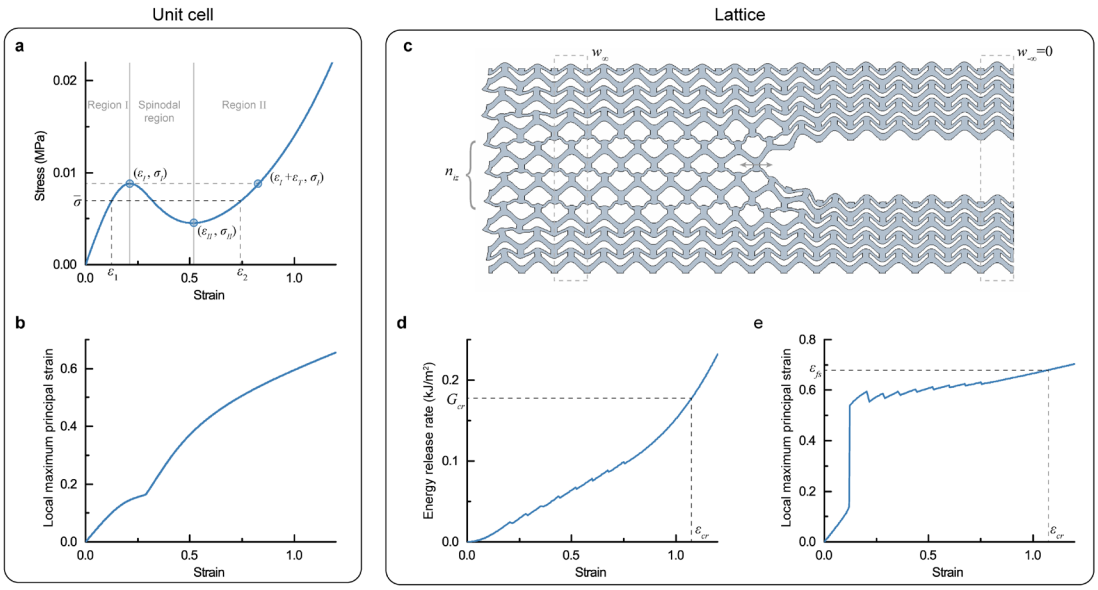

Supplementary Fig. 4 | Theoretical model. a, Stress-strain curve of the unit cell with t_s/l=0.10, obtained from FE simulation. **b**, Local maximum principal strain in the unit cell with t_s/l=0.10, obtained from FE simulation. **c**, Schematic of a lattice structure with a precrack. **d**, Theoretically predicted relationship between energy release rate and strain during loading. **e**, Theoretically predicted variation of local maximum principal strain with strain during loading.

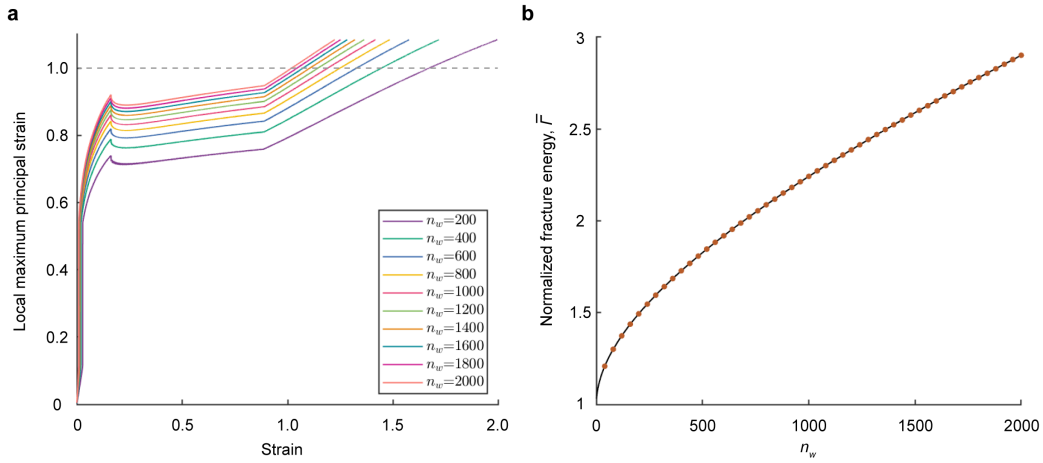

Supplementary Fig. 5 | Theoretical predictions of fracture energy. a, Local maximum principal strain in the metamaterial during loading, as predicted by the theoretical model. **b**, Predicted fracture energy versus sample size, assuming the fracture strain of the constituent material is set to 1.0, ensuring extrinsic fracture toughness for all samples. The fracture energy is normalized by C_2^2.

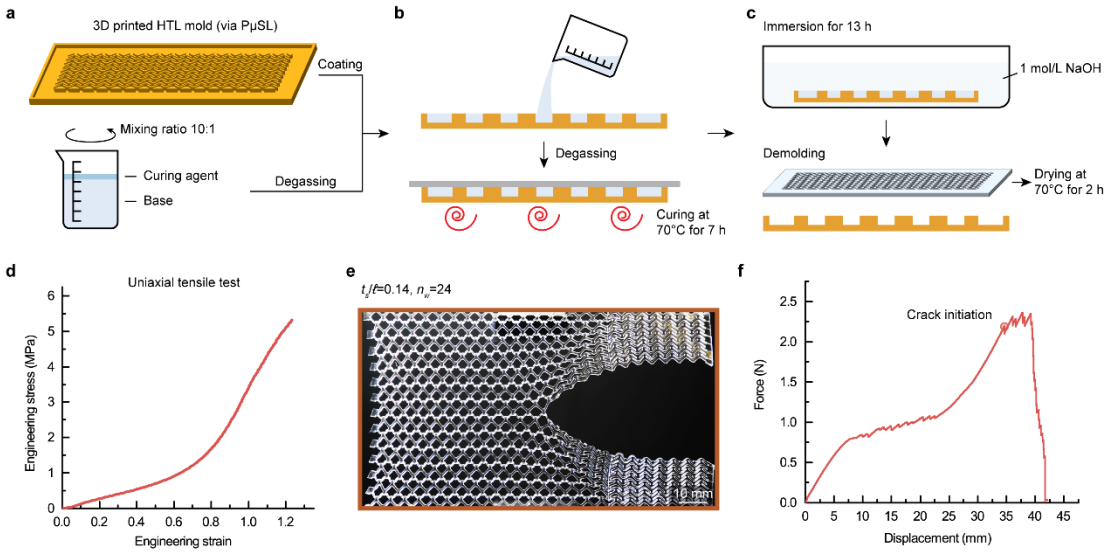

Supplementary Fig. 6 | Fabrication using sodium hydroxide (NaOH) immersion for demolding. a, Schematic illustration of the mold printing and precursor preparation process. **b**, Schematic of the curing step. **c**, Schematic of the demolding step. Samples can be easily peeled from the HTL molds after immersion in a sodium hydroxide solution, as the HTL molds slightly dissolve and the samples undergo slight swelling. This method enables a relatively high fracture strain of the constituent material and easy demolding when curing at 70°C. However, at higher curing temperatures, the samples may be damaged during demolding due to increased brittleness. **d**, Representative stress-strain curve of a solid tensile specimen fabricated using the NaOH immersion method. The material exhibits an engineering fracture strain of ~1.23 and corresponding logarithmic fracture strain of ~0.80. **e**,**f**, Image captured just before the onset of fracture and the corresponding force-displacement curve of a metamaterial with t_s/l =0.14 and n_w=24, fabricated using the NaOH immersion method.

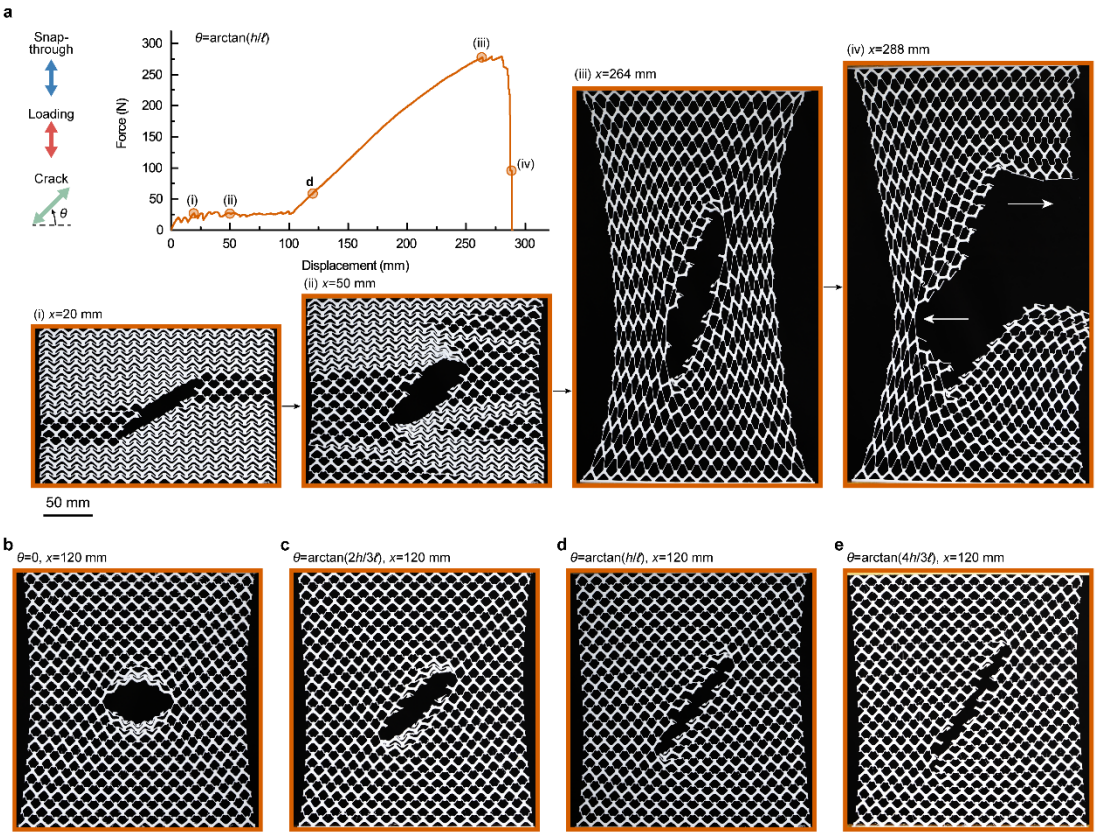

Supplementary Fig. 7 | Fracture behaviors of curved-beam metamaterials (n_w=n_h=16) with inclined precracks. a, Force-displacement curve and corresponding snapshots during loading of a metamaterial containing a precrack with inclined angle θ=arctan(h/l). **b-e**, Snapshots at the same displacement for metamaterials with precracks with inclined angles of θ=0, arctan(2h/3l), arctan(h/l), and arctan(4h/3l), respectively.

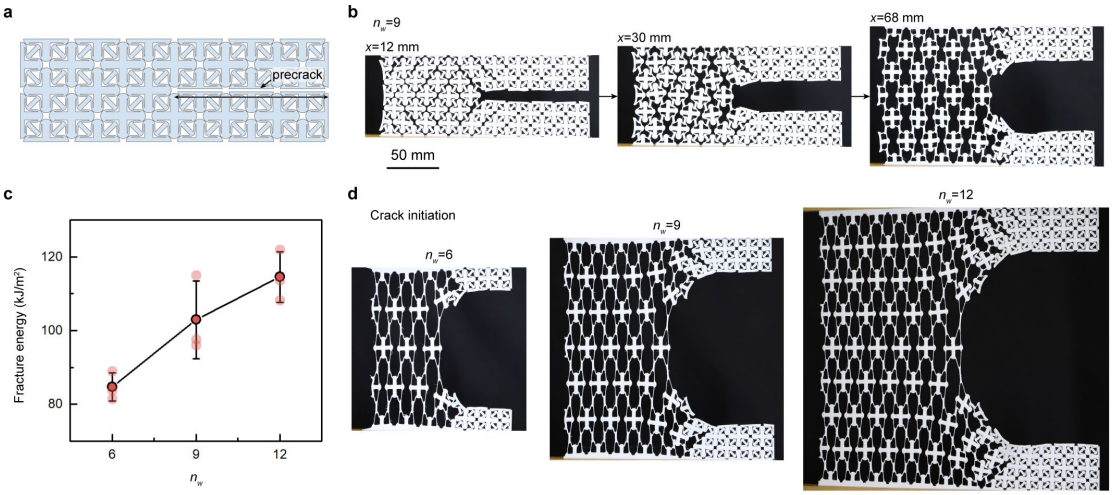

Supplementary Fig. 8 | Fracture energy and size dependence of metamaterials exhibiting bidirectional snap-through instabilities not aligned with the loading direction. a, Schematic of an edge-cracked sample. **b**, Snapshots during loading of the edge-cracked sample with n_w=9. **c-d**, Fracture energy and snapshots at crack initiation for samples with varying sizes.

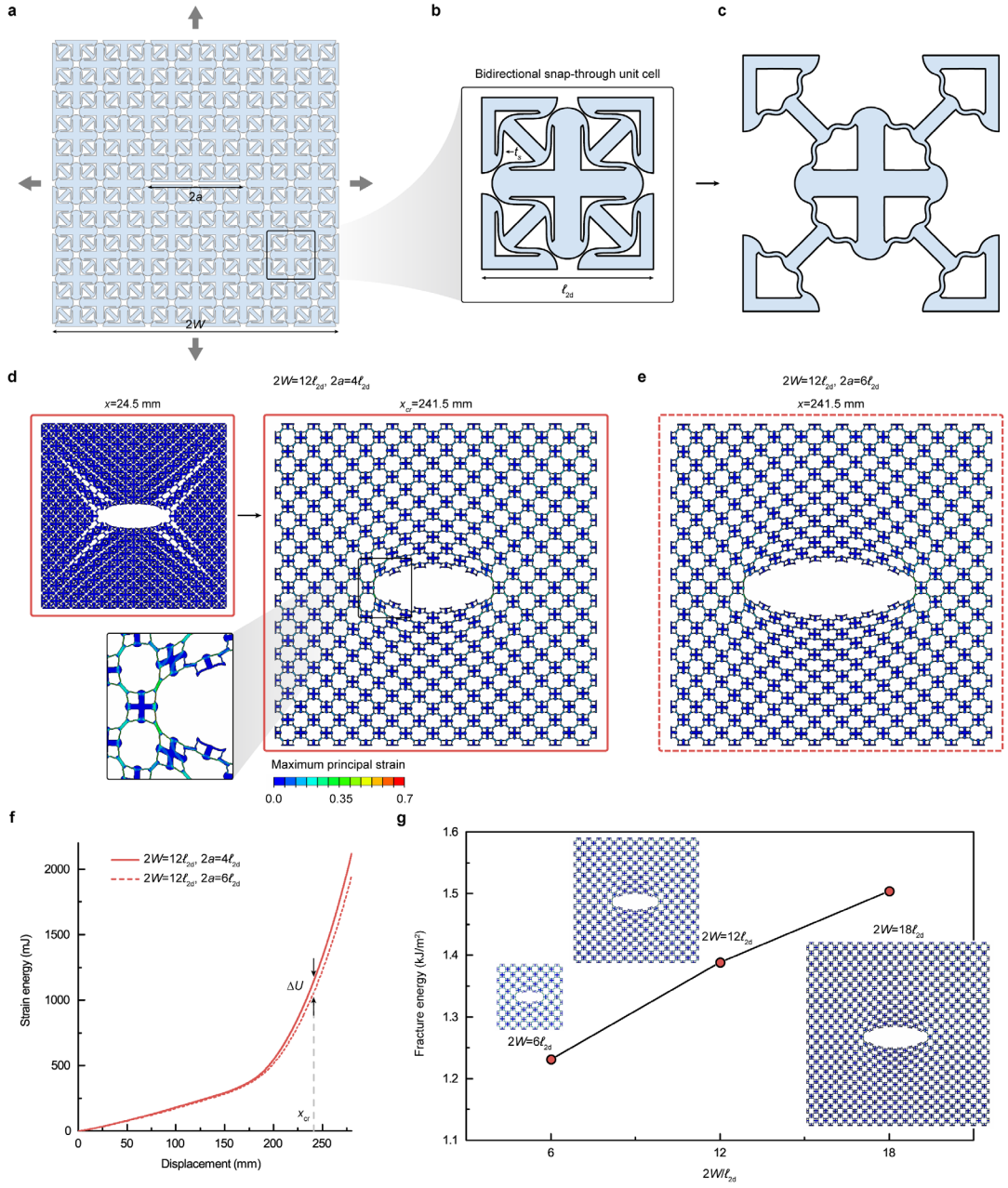

Supplementary Fig. 9 | Fracture behaviors of bidirectional snap-through metamaterials under biaxial tension. a, Schematic of a center-cracked bidirectional snap-through metamaterial. **b**, Geometry of the 2D unit cell exhibiting snap-through instability along diagonal directions. **c**, Deformed configuration of the unit cell under biaxial tension. **d**, Snapshots during biaxial tension of a bidirectional snap-through metamaterial with sample width $2W=12l_{2d}$ and crack length $2a=4l_{2d}$. Snap-through instabilities are first triggered from the crack tip and then propagate throughout the

sample. The critical displacement is defined as the point at which the local maximum principal strain reaches the fracture strain of the base material. **e**, A reference sample with a larger crack length ($2a=6l_{2d}$) loaded to the same displacement. **f**, Strain energy versus displacement curves for two metamaterial samples with the same size $2W=12l_{2d}$ but different crack lengths of $2a=4l_{2d}$ and $2a=6l_{2d}$. Fracture energy is calculated as the strain energy difference between the two samples at the critical displacement of the sample with $2a=4l_{2d}$, divided by the difference in crack area. **g**. Fracture energy as a function of sample size for bidirectional snap-through metamaterials subjected to biaxial tension.

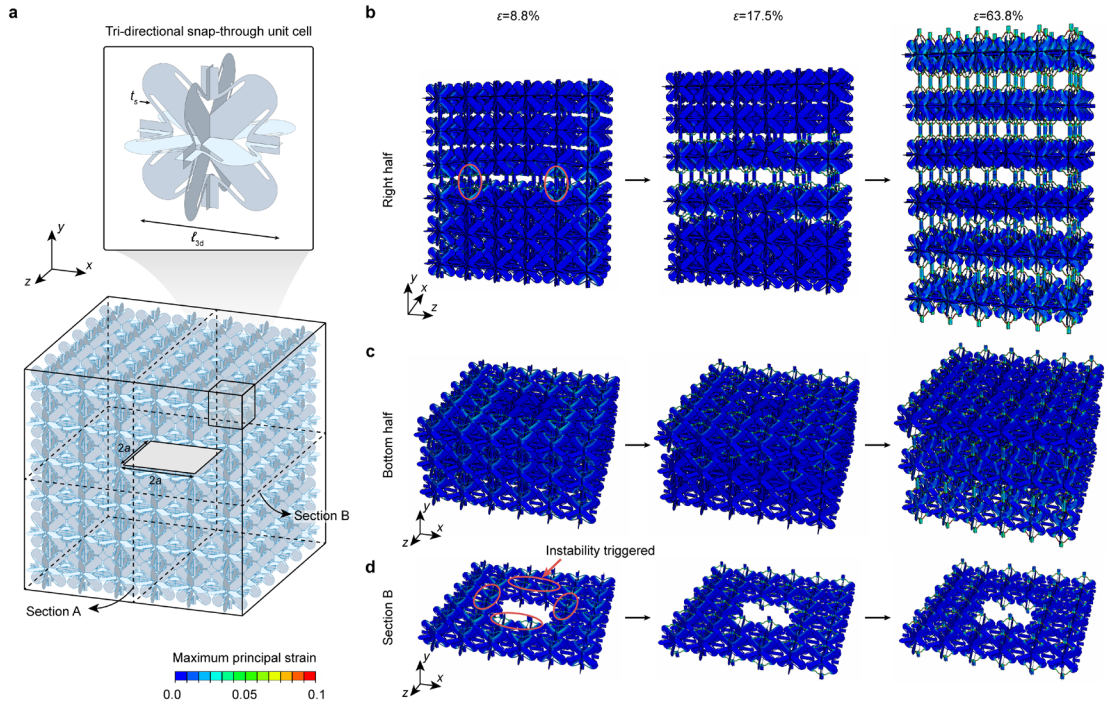

Supplementary Fig. 10 | Fracture behaviors of a 3D metamaterial exhibiting tri-directional snap-through instabilities. a, Geometry of the 3D unit cell and schematic of a 3D metamaterial sample containing an embedded square crack. **b**, Snapshots during loading of the right half of the metamaterial, sectioned along plane A and viewed from the negative *x*-axis. **c**, Snapshots during loading of the bottom half of the metamaterial, sectioned along plane B. **d**, Snapshots during loading of the layer of unit cells located at section B.

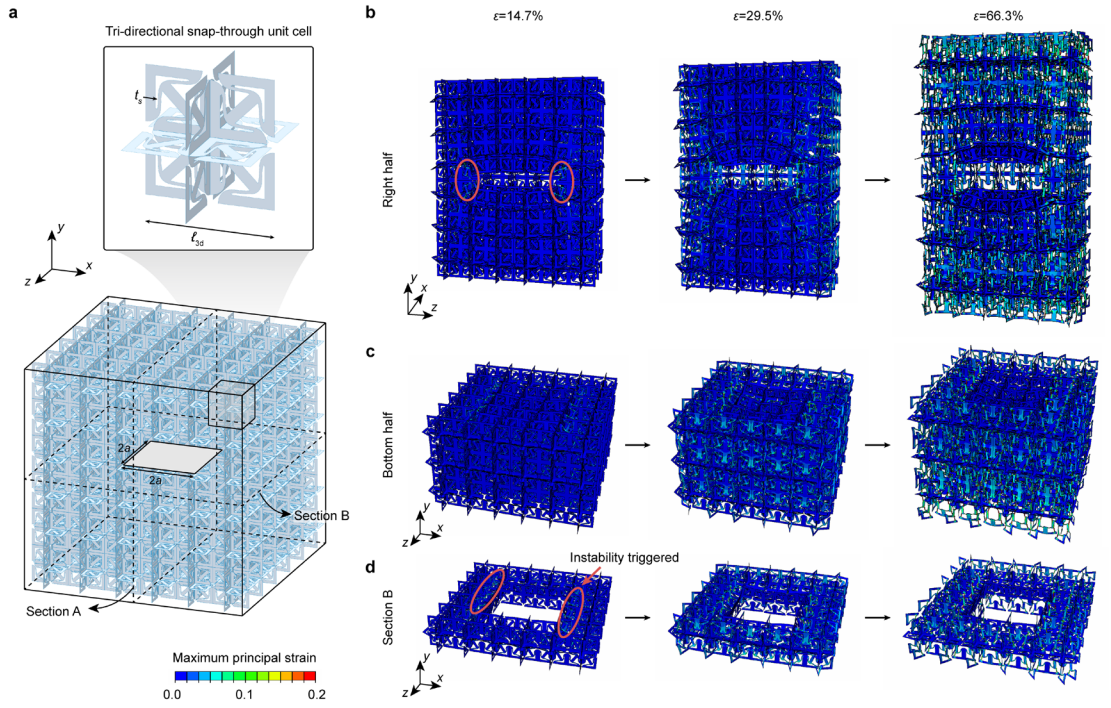

Supplementary Fig. 11 | Fracture behaviors of a 3D metamaterial exhibiting tri-directional snap-through instabilities not aligned with the loading direction. a, Geometry of the 3D unit cell and schematic of a 3D metamaterial sample containing an embedded square crack. **b**, Snapshots during loading of the right half of the metamaterial, sectioned along plane A and viewed from the negative *x*-axis. **c**, Snapshots during loading of the bottom half of the metamaterial, sectioned along plane B. **d**, Snapshots during loading of the layer of unit cells located at section B.

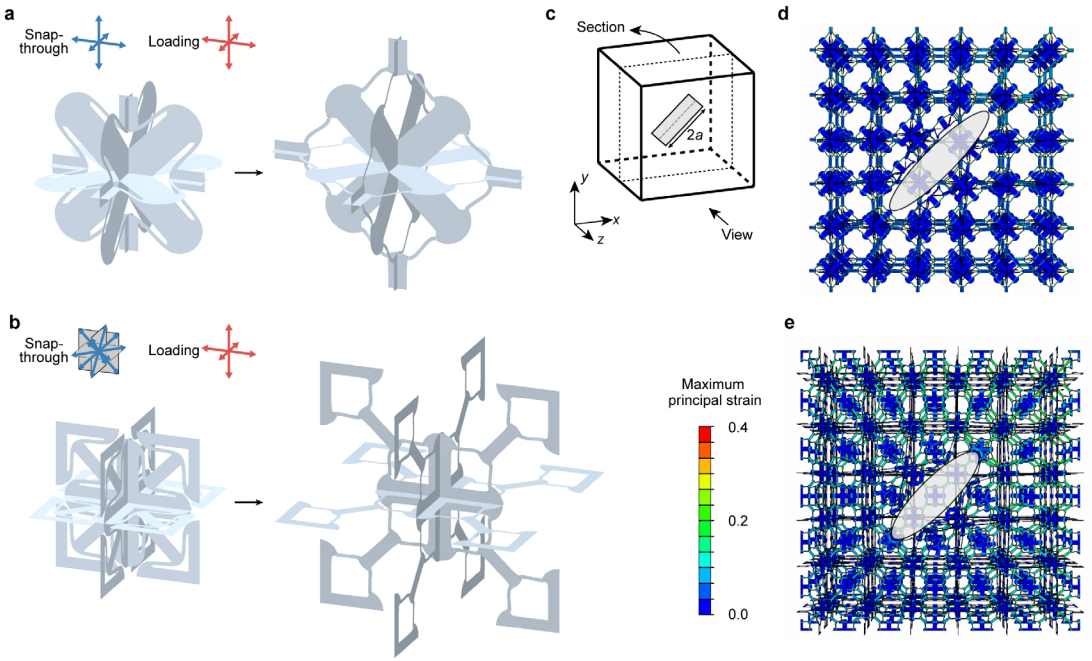

Supplementary Fig. 12 | Fracture behaviors of tri-directional snap-through metamaterials under tri-axial tension. a-b, Geometry of the 3D unit cells exhibiting snap-through instabilities along three directions and their deformed configurations under tri-axial tension. **c**, Schematic of the 3D sample containing an embedded inclined square crack. **d-e**, Snapshots during loading of the back half of these metamaterials, viewed from the positive *z*-axis.

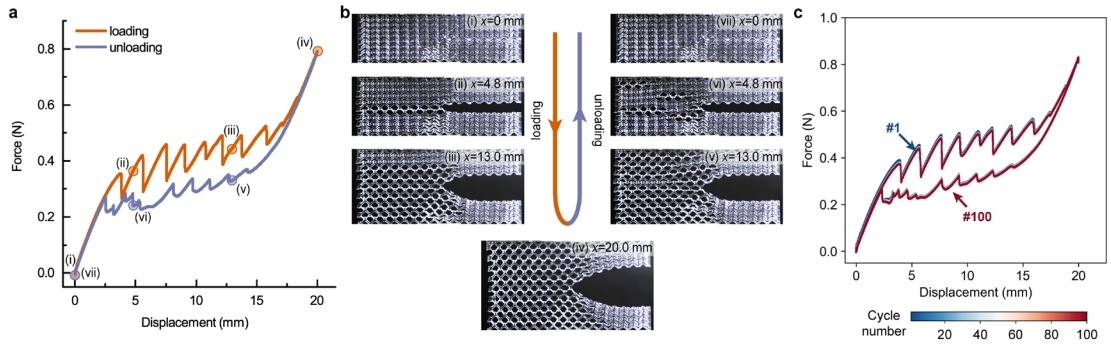

Supplementary Fig. 13 | Experimental unloading and cyclic loading behavior of the pre-cracked metamaterial. **a**, Force-displacement curve during loading and unloading. **b**, Snapshots illustrating the reversibility of the pre-cracked metamaterial during unloading. **c**, Force-displacement curves over 100 loading cycles.

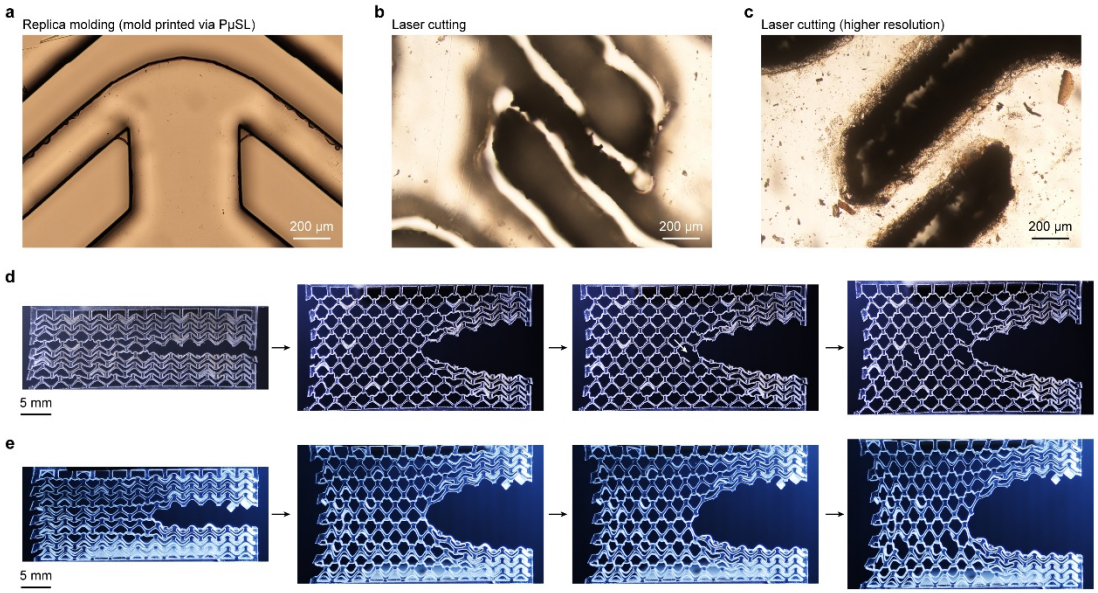

Supplementary Fig. 14 | Comparison of fabrication via laser cutting. a-c, Optical microscope images of samples fabricated through molding, laser cutting, and high-resolution laser cutting, respectively. **d**,**e**, Snapshots during loading of samples fabricated via laser cutting. The results indicate that laser cutting introduces significant defects and variations in beam thickness. As a result, instability or fracture may not consistently initiate from the crack tip.

Supplementary Table 1. Fitting parameters of the scaling law for fracture energy versus the number of unit cells.

Material	Unit cell	C_1 ($\sqrt{kJ/m^2}$)	C_2 ($\sqrt{kJ/m^2}$)
PDMS (T_2=70°C)	Curved beam (l=5 mm)	0.0490	0.243
PDMS (NaOH)	Curved beam (l=3 mm)	0.0569	0.317
TPU	Curved beam (l=15 mm)	0.948	4.26
TPU	3D straw-like shell	0.220	0.579

Supplementary References

1. Overvelde, J. T., Kloek, T., D'Haen J, J. & Bertoldi, K. Amplifying the response of soft actuators by harnessing snap-through instabilities. *Proc. Natl Acad. Sci. USA* **112**, 10863–8 (2015).
2. Ni, B. & Gao, H. Engineer energy dissipation in 3D graphene nanolattice via reversible snap-through instability. *J. Appl. Mech.* **87**, 031012 (2020).
3. Puglisi, G. & Truskinovsky, L. Mechanics of a discrete chain with bi-stable elements. *J. Mech. Phys. Solids* **48**, 1–27 (2000).
4. McMeeking, R. M. & Evans, A. G. Mechanics of transformation-toughening in brittle materials. *J. Am. Ceram. Soc.* **65**, 242–246 (1982).
5. Anderson, T. L. *Fracture Mechanics: Fundamentals and Applications*. (CRC press, 2017).
6. Gibson, L. J. & Ashby, M. F. *Cellular Solids: Structure and Properties*. (Cambridge University Press, 1999).